

# Fano Resonance and Incoherent interlayer excitons in molecular van der Waals heterostructures

Carlos R. Lien-Medrano<sup>1</sup>, Franco P. Bonafé<sup>2</sup>, Chi Yung Yam<sup>3</sup>,

Carlos-Andres Palma<sup>4,5,\*</sup>, Cristián G. Sánchez<sup>6,†</sup> and Thomas Frauenheim<sup>3,1</sup>

<sup>1</sup>*Bremen Center for Computational Materials Science, Universität Bremen, Bremen, Germany*

<sup>2</sup>*Max Planck Institute for the Structure and Dynamics of Matter, Hamburg, Germany*

<sup>3</sup>*Shenzhen JL Computational Science and Applied Research Institute (CSAR), Shenzhen, China*

<sup>4</sup>*Institute of Physics, Chinese Academy of Sciences; Beijing, P.R. China.*

<sup>5</sup>*Department of Physics & IRIS Adlershof, Humboldt-Universität zur Berlin, Berlin, Germany*

<sup>6</sup>*Instituto Interdisciplinario de Ciencias Básicas, Universidad Nacional de Cuyo, Mendoza, Argentina and*

<sup>7</sup>*Beijing Computational Science Research Center, Beijing 100193, China*

(Dated: April 23, 2022)

We employ an adapted Gersten-Nitzan model and real time time-dependent density functional tight-binding to study the optoelectronics of self-assembled monolayers on graphene nanoribbons. We find Fano resonances that cause electromagnetic induced opacity and transparency, and reveal an additional incoherent process leading to interlayer exciton formation with a characteristic charge transfer rate. These results showcase hybrid van der Waals heterostructures as paradigmatic 2D optoelectronic stacks, whereby molecular-scale effects could lead to advanced optics or tunable charge transfer for photovoltaics.

Molecular Photosensitizing is a fundamental process in optoelectronics material design. This has led to important advancements in lasing, light emitting diodes and photovoltaic cells [1–6]. At the same time, van der Waals (vdW) heterostructures have demonstrated avant-garde optical properties, bearing promise in conception and design of photomodulators, photovoltaic elements [7–9], and bare potential for advanced optical elements, such as antireflection coatings and cooling filters [10]. In principle, vdW heterojunctions with marginal adsorption and efficiency [11], may be stacked to achieve photovoltaic efficiencies higher than state-of-the art tandem perovskites [12].

While gating and doping in two-dimensional (2D) materials is well-known [11, 13–21], the physics of photosensitizing and advanced optical properties have not been fully investigated [22, 23], especially in the context of molecular vdW heterostructures (MVs), that is, regular monolayer stacks on 2D materials. Because self-assembled architectures at interfaces grant a high degree of bottom-up control [24, 25], a modular and layered approach could be envisaged towards technologically relevant properties, such as photovoltaics, optical switching, lasing and parametric amplification. Just recently for instance, we have shown photoresponsive sensitizers for graphene [11]. The resulting optoelectronic element displayed peak incident photon to current efficiencies of 0.6%, corresponding to apparent maximum efficiency for the monolayer-thin absorber. Such high responses from monolayers motive further study into the mechanism of photo-induced charge transport and related properties at

interfaces.

Moreover, nanographenes and graphene nanoribbons (GNRs) are currently some of the most optically relevant materials for interfacial self-assembly [26], featuring broadband absorption [27], electron mobility modulation [28], single-photon emission [29] to mention a few. With accurate computational tools rapidly evolving to handle complex molecular systems, the prototyping of sophisticated sensitized vdW architectonics could become viable. On the other hand, it is well known that the coupling of a discrete localized state to a continuum of states gives rise to a very special phenomenon in optics, the Fano resonance [30]. This has been used to describe resonant phenomena in several systems such as photonic crystals, superconductors and plasmonic nanoantennas [31–33]. While MVs have all the necessary elements to show Fano effects in their optical properties, so far this fact has not been investigated.

To model electronic structure we employ the self-consistent-charge density functional tight binding method (SCC-DFTB). The SCC-DFTB Hamiltonian is based on a second-order expansion of the full Kohn-Sham energy with respect to electronic density fluctuations. This method has proved accurate for the description of quantum properties and electronic structures in large organic systems [34–36]. In particular, we have used the DFTB+ package implementation of the SCC-DFTB method [37]. Here we explore the novel optical features of MVs in which Fano resonances play a key role. Namely, we have computationally studied the optical properties of broad armchair graphene nanoribbon (AGNR) sensitized by a self-assembled monolayer of rylene dyes (TDI) acceptors by real time time-dependent density functional tight-binding (TD-DFTB) simulations. Our computational framework [38] grants access to the study of nonlinear excitations in systems of thousands of atoms within femto and picosecond timescales. The simulated spec-

\* Corresponding author.  
palma@palmaland.edu

† Corresponding author.  
csanchez@mendoza-conicet.gob.ar

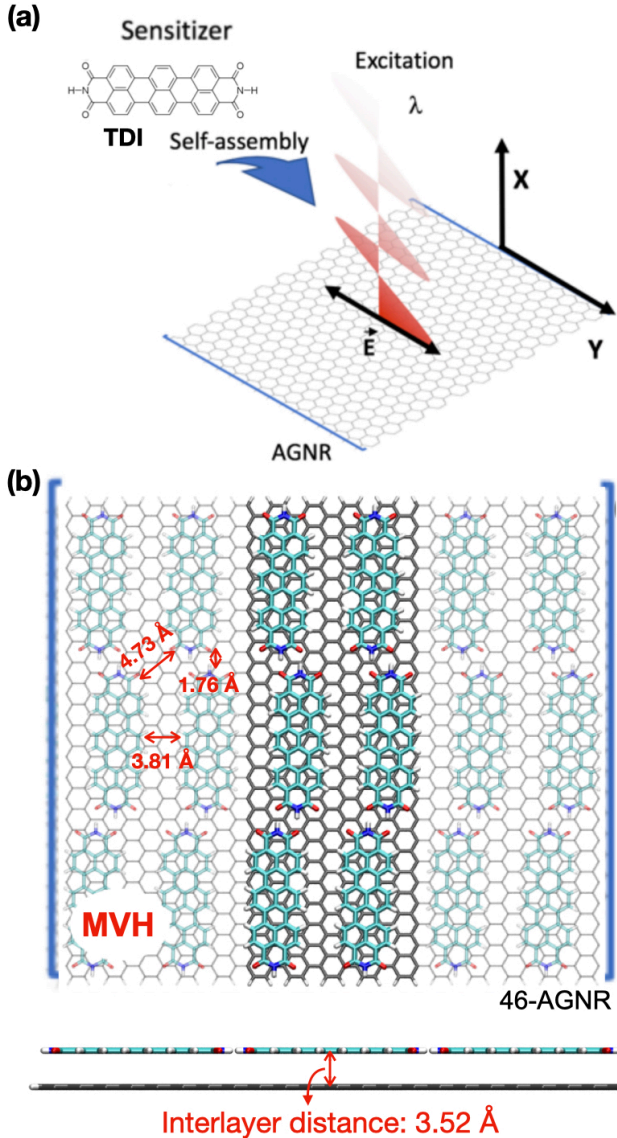


FIG. 1. Schematic diagram of the studied structure. (a) Scheme of the molecular vdW heterostructures proposed by self-assembly of Terrylene carboxylic diimide (TDI) as monolayer-sensitizer on 1D Armchair Graphene Nanoribbon platform. The external field applied for excitation in the Y axis (non-periodic direction of the ribbon) is also represented. (b) Monolayer of TDI molecules on top of a 46 atoms width armchair graphene nanoribbon (46-AGNR) as the model heterostructure used for the calculations. The unit cell (showing thicker bonds) is composed by six TDI molecules interacting by Hydrogen bonds between them on top of the 46-AGNR with a total of 804 atoms. Characteristic distances are depicted in the Figure, particularly, the interlayer distance between monolayer and platform is 3.52 Å.

tra of the vdW heterostructure shows a remarkable Fano resonance when compared to the isolated components. This is an universal, classical effect of the stacked molecular vdW systems as a result of coupled dipoles, and hence it can be atomically engineered to produce novel,

on-demand transparent and particularly IR-transparent photovoltaic elements for solar cells, demonstrating that self-cooling active layers are possible. In addition to the Fano shape for the in-plane response, the out-of-plane response shows non-classical features given by interlayer charge transfer, which can be interpreted as incoherent exciton formation as a decay route of in-plane excitations. Our findings strongly suggest that nonlinear interlayer exciton formation is a universal property of self-assembled monolayers at nanosized vdW interfaces which can be tuned at will. The broad armchair graphene nanoribbon 46-AGNR is a small-gap (0.1 eV) semiconductor with absorptivity near 5% 1.0-3.5 eV along the aperiodic  $[\Gamma\text{-}M]$  direction (see Supplemental Material Fig. S1). The 46-AGNR is used as the graphene-like platform for this study. We focus on one representative self-assembly configuration and sensitizer on top of 46-AGNR (Fig. 1), using terrylene diimide (TDI) [11]. For the remainder of this work we have considered a self-assembled configuration of TDI as depicted in Fig. 1(b).

We have simulated the absorption spectra via density matrix propagation within TD-DFTB, as explained in ref. 38 (for more details on the computational methods please refer to the Materials and methods section of the Supplemental Material). While TD-DFTB neglects many-body effects and exciton binding energies it provides an accurate description for the absorption spectrum of benzenoid ribbons [39] and broad AGNRs.

The calculated spectra reveal absorption suppression or enhancement upon adsorption of the sensitizers around the dye energy excitation, when compared to the sum of the absorption of the separate components (Fig. 2(a)). An absorption maximum of 692 nm is found for the monolayer on the AGNR platform (cf. 735 nm dye excitation on graphene [11]). Removal of the underlying graphene platform blueshifts the absorption peak position by 13 nm, to 679 nm.

The spectral features of the combined system can be resolved in  $k$ -space, as depicted in Figs. 2(b), (c) and (d). Here, we show a momentum resolved snapshot of the time-dependent electron population distribution at 96 fs, projected on the ground state bands for 3 different excitation energies: 1.5 eV (2(b), suppression/transparency), 1.78 eV (2(c), dye excitation, ) and 2.1 eV (2(d), enhancement/opacity). The MVH as well as its separate components are considered for the plots. Red (blue) circles denote the increase (decrease) of electron occupation, and the circle size is proportional to the change of population. The fundamentals of this method can be found in refs [38, 40]. The absorption suppression of the heterostructure at 1.5 eV agrees with a reduction of population change with respect to the free platform (Fig 2(b)). The opposite behaviour is depicted in Figure 2(d), where the heterostructure shows an increase of the population change with respect to the free platform, in concordance with the absorption enhancement at 2.1 eV. Furthermore, the population change at 1.78 eV shown in Fig. 2(c) is clearly quenched with respect to the free standing mono-

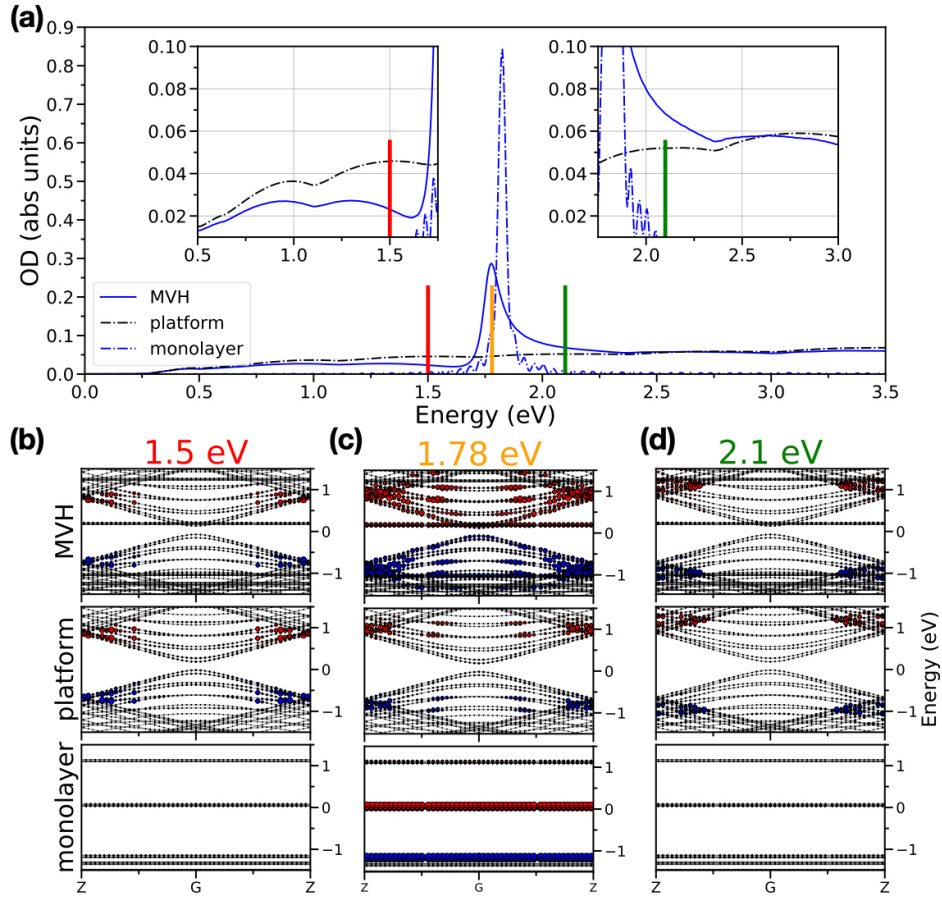


FIG. 2. Theoretical absorption spectrum of MVH and band population analysis of the Fano features. (a) Simulated absorption spectra for the MVH studied and its separate components (ribbon platform and dyes monolayer). (b), (c) and (d) present the band populations under continuous excitation at three different energies, 1.5, 1.78 and 2.1 eV respectively. Red (blue) circles denote the increase (decrease) of electron occupation and the circle size is proportional to the change of population. In order to see the differences, all cases show first the composed heterostructure and then the separate components. The excitations were performed using a continuous laser perturbation tuned with the energy of interest. For all the band populations the snapshot frame was taken at 96 fs of the electron dynamics simulation.

layer. The population change involving different states than those of the separate system in Fig. 2(c) is also evidence of novel interlayer transitions (vide infra). It is also proven here that the suppression and enhancement effect on the absorption depends on the coverage degree of the platform as shown in Fig. S2 for a range of TDI submonolayers.

It is well known that the monolayer electronic structure can be described by molecular energy levels (without dispersion), while the platform has a wide and relatively flat (or quasi-linear) absorption over a broad range of energies from the UV to the IR region which include those of the monolayer excitation in the visible. These two facts are textbook conditions for a Fano resonance [41]. To shed light on the origin of the Fano resonance present in 2(a), we used an adapted Gersten-Nitzan (aGN) model to calculate the polarizability of the heterostructure from the polarizabilities of the separate components. The well-known Gersten-Nitzan model [42]

has been used successfully over 40 years in the realm of surface-enhanced Raman spectroscopy to calculate radiative and non-radiative decay rates of molecules adsorbed on metals [43–45]. The basic setup considered for the model are two point dipoles, each of them coupled to the external field, and to the dipolar field generated by the other system up to first order, neglecting image field effects, as depicted in Fig. 3(a).

The effect of the dipolar coupling between the systems in such setup can be described by an effective polarizability (see Supplemental Material for formal definition), which for system A reads:

$$\alpha^{\text{eff},A} = \alpha^A(\omega) + \alpha^A(\omega)D\alpha^B(\omega), \quad (1)$$

where

$$D = \frac{1}{4\pi\epsilon_0 R_{AB}^3} \begin{pmatrix} 2 & 0 \\ 0 & 1 \end{pmatrix} \quad (2)$$

is the geometric factor for two point dipoles separated

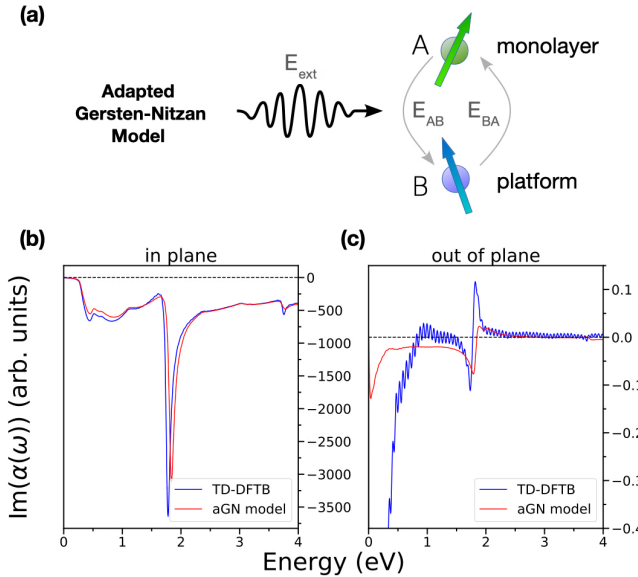


FIG. 3. Adapted Gersten-Nitzan Model and Comparison with TD-DFTB results. (a) Simple model representation of two point dipoles interacting with each other via dipolar field and with an external field. (b) In-plane imaginary component of the Polarizability tensor obtained from the adapted GN model and TD-DFTB simulations for the MVH. (c) Out-of-plane imaginary component of the Polarizability tensor obtained from the adapted GN model and TD-DFTB simulations of MVH. The imaginary part of the in-plane component is related to the absorption spectrum presented in Figure 2 and clearly shows the Fano shape.

at (interlayer) distance  $R_{AB}$ . Exchanging indices A and B gives the equivalent formula for system B. The total polarizability is the sum of both.

The polarizabilities used as input for the model were calculated for the separate systems in vacuum using real time TD-DFTB (see Fig. S3). The imaginary part of the in-plane (**ip**) (y-axis response from y-polarized field) polarizability calculated from the aGN model (Fig. 3(b)) shows a Fano resonance around 1.78 eV. When a broadening of 13 fs is added to the monolayer polarizability (*vide infra*), the curve obtained agrees quantitatively with the one calculated for the full combined system using TD-DFTB (same Fig. 3(b)). This proves that the **ip** transparency/enhancement arises fundamentally from a dipolar coupling between the systems. However, the out-of-plane (**oop**) (y-axis response for x-polarized field) polarizability calculated from the aGN model (Fig. 3(c)) agrees only qualitatively with the TD-DFTB one.

In order to gain insight into the **oop** process, we studied the electron dynamics upon photoexcitation of the dye resonance in the **ip** direction. Figure 4(a) shows the **ip** dipole moment  $\mu_y(t)$  for different field strengths. The **ip** dipole moment grows linearly during the first steps (up to approximately 20 fs) and then reaches a stationary state showing a saturation value that depends on the field strength. The amplitudes of the different  $\mu_y(t)$  were

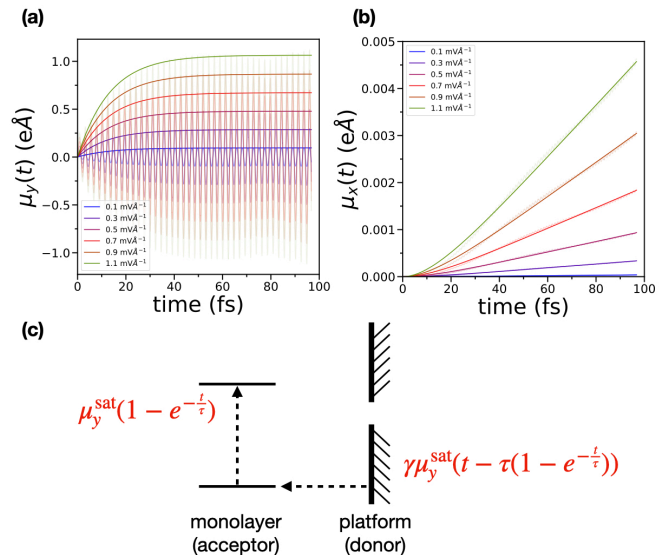


FIG. 4. Time dependent analysis of dipole moments with respect to the field strength  $E_0$ . (a) In plane dipole moment ( $\mu_y$ ) vs. time for different  $E_0$  values. (b) Out of plane dipole moment ( $\mu_x$ ) vs. time for different  $E_0$  values. (c) Schematic representation of the two process involved, photoexcitation of dye molecules and charge transfer to the ribbon platform (exciton formation). The mathematical expressions used for fitting dipole curves in A and B are presented as well. All the excitations were performed at 1.78 eV (dye excitation energy).

fitted following the expression:

$$\mu_y^{\text{fit}} = \mu_y^{\text{sat}}(1 - e^{-\frac{t}{\tau}}), \quad (3)$$

where  $\mu_y^{\text{sat}}$  is the saturation dipole moment, which is directly proportional to the field strength  $E_0$ , and  $\tau$  is the characteristic lifetime of the saturation process with a constant value of 13 fs. In the linear response regime, a linear growth of the dipole moment in time would be expected. The observed saturation is an evidence of a dissipation process after the photoexcitation of the dye molecules. Fig. 4(b) shows the **oop** dipole moment  $\mu_x$  as a function of time for the same dynamics in Fig. 4(a). The  $\tau$  value obtained from the fitted curves was used as the broadening of the **ip** molecular polarizability in 3(b). This broadening is essential for the quantitative agreement between the aGN model and the full quantum results and shows the existence of a decay channel for the molecular excitation.

The appearance of an **oop** dipole moment indicates the cause decay of the excitation is interlayer charge transfer (CT) from the platform to the monolayer. The dipole moment  $\mu_x(t)$  was fitted to the following expression (the time integral of equation 3):

$$\mu_x^{\text{fit}} = \gamma \mu_y^{\text{sat}}(t - \tau(1 - e^{-\frac{t}{\tau}})), \quad (4)$$

where  $\mu_y^{\text{sat}}$  and  $\tau$  are the same as in equation 3 and  $\gamma$  represents the charge leaking between both systems and

depends linearly on  $E_0$  (so does  $\mu_y^{\text{sat}}$ ). The value of charge transferred  $q_{CT}^{\text{fit}}$  can be obtained from eq. 4 dividing by the interlayer distance between the monolayer and the platform:

$$q_{CT}^{\text{fit}} = \mu_x^{\text{fit}} / R_{AB}. \quad (5)$$

Figure S4 shows that the  $\Delta q(t)$  obtained from the simulation agrees with the results from equation 5 with  $R_{AB}$  approximately equal to the interlayer distance shown in Fig. 1. The CT process explains the differences from Fig. 3(c), as the aGN model cannot account for charge leaking. Hence, continuous wave excitation of the **ip** mode decays into incoherent interlayer excitons in which a net **oop** dipole moment is caused by tunnelling of electrons from the platform to the monolayer. Upon closer inspection of the band diagrams in Fig. 2(b) (see Fig. S5), avoided crossings can be seen for the HOMO and HOMO-1 orbitals of the monolayer. The avoided crossings explain the direction of charge transfer, as only the occupied frontier orbitals from the molecule are mixed with the substrate, establishing a clear channel for charge leakage from the platform into partially depopulated monolayer states. Once the linear regime has been established in the **oop** dipole moment charge transfer current reaches a steady state. This current is linear with illumination intensity (see figure S6) with a slope (photoresponse) of  $1.3 \text{ mA W}^{-1}$ . It is important to note that the observed **oop** dipoles always develop in interlayer excitons [46, 47] and can be harnessed for exciton dissociation.

In summary, we have found evidence of induced transparency and opacity of the substrate arising from a Fano spectral shape upon formation of the MVH architecture.

This spectral change is a general feature of these types of systems, and can already be captured by a simple module of electrostatically interacting dipoles, which is valid even for the interplanar distances at equilibrium. This simple model cannot capture, however, the bandwidth of the response calculated from a fully atomistic, quantum-dynamical treatment of the system which is given by the lifetime of a new decay channel. Our time-resolved carrier dynamics simulations suggest that such a process could be understood as the formation of an incoherent exciton. These results open a path for improved design of on-demand, wide-band-absorbing modular multilayer organic PV devices and for engineering new atomic-scale metamaterials with highly tunable optical properties.

C.R.L.-M. acknowledges the support from the DFG-RTG2247 grant (RTG-QM3 Program) for the post-doctoral fellowship and the high-computing resources of the BCCMS, University of Bremen. F.P.B. acknowledges financial support from the European Union's Horizon 2020 research and innovation programme under the Marie Skłodowska-Curie grant agreement no. 895747 (NanoLightQD). C.-A.P. acknowledges support from the NSFC China (nos. 51325204 and 51761135130), the CAS Bureau of Frontier Sciences and Education no. QYZDB-SSW-SLH038 and CAS Strategic Priority Research Program XDB33000000 the Cluster of Excellence "Matters of Activity" funded by the DFG under Germany's Excellence Strategy - EXC 2025 - 390648296 and Alexander von Humboldt Foundation. C.G.S acknowledges financial support by Consejo Nacional de Investigaciones Científicas y Técnicas (CONICET) through Grant PIP 112-2017-0100892CO and Agencia Nacional de Promoción Científica y Tecnológica (ANPCYT) through grant PICT-2017-1605.

- 
- [1] J. Burschka, N. Pellet, S.-J. Moon, R. Humphry-Baker, P. Gao, M. K. Nazeeruddin, and M. Grätzel, Sequential deposition as a route to high-performance perovskite-sensitized solar cells, *Nature* **499**, 316 (2013).
- [2] K. Vandewal, K. Tvingstedt, A. Gadisa, O. Inganäs, and J. V. Manca, Relating the open-circuit voltage to interface molecular properties of donor:acceptor bulk heterojunction solar cells, *Physical Review B* **81**, 125204 (2010).
- [3] D. Qian, Z. Zheng, H. Yao, W. Tress, T. R. Hopper, S. Chen, S. Li, J. Liu, S. Chen, J. Zhang, X.-K. Liu, B. Gao, L. Ouyang, Y. Jin, G. Pozina, I. A. Buyanova, W. M. Chen, O. Inganäs, V. Coropceanu, J.-L. Bredas, H. Yan, J. Hou, F. Zhang, A. A. Bakulin, and F. Gao, Design rules for minimizing voltage losses in high-efficiency organic solar cells, *Nature Materials* **17**, 703 (2018).
- [4] I. Ramirez, M. Causa', Y. Zhong, N. Banerji, and M. Riede, Key Tradeoffs Limiting the Performance of Organic Photovoltaics, *Advanced Energy Materials* **8**, 1703551 (2018).
- [5] Y. Liu, J. Zhao, Z. Li, C. Mu, W. Ma, H. Hu, K. Jiang, H. Lin, H. Ade, and H. Yan, Aggregation and morphology control enables multiple cases of high-efficiency polymer solar cells, *Nature Communications* **5**, 5293 (2014).
- [6] J. Yuan, Y. Zhang, L. Zhou, G. Zhang, H.-L. Yip, T.-K. Lau, X. Lu, C. Zhu, H. Peng, P. A. Johnson, M. Leclerc, Y. Cao, J. Ulanski, Y. Li, and Y. Zou, Single-Junction Organic Solar Cell with over 15% Efficiency Using Fused-Ring Acceptor with Electron-Deficient Core, *Joule* **3**, 1140 (2019).
- [7] D. Jariwala, T. J. Marks, and M. C. Hersam, Mixed-dimensional van der Waals heterostructures, *Nature Materials* **16**, 170 (2017), 1608.00515.
- [8] M. Buscema, J. O. Island, D. J. Groenendijk, S. I. Blanter, G. A. Steele, H. S. J. v. d. Zant, and A. Castellanos-Gomez, Photocurrent generation with two-dimensional van der Waals semiconductors, *Chemical Society Reviews* **44**, 3691 (2015), 1506.00679.
- [9] G. A. Ermolaev, D. V. Grudinin, Y. V. Stebunov, K. V. Voronin, V. G. Kravets, J. Duan, A. B. Mazitov, G. I. Tselikov, A. Bylinkin, D. I. Yakubovsky, S. M. Novikov, D. G. Baranov, A. Y. Nikitin, I. A. Kruglov, T. Shegai, P. Alonso-González, A. N. Grigorenko, A. V. Arsenin, K. S. Novoselov, and V. S. Volkov, Giant optical anisotropy in transition metal dichalcogenides for next-

- generation photonics, *Nature Communications* **12**, 854 (2021), 2006.00884.
- [10] M. ElKabbash, T. Letsou, S. A. Jalil, N. Hoffman, J. Zhang, J. Rutledge, A. R. Lininger, C.-H. Fann, M. Hinczewski, G. Strangi, and C. Guo, Fano-resonant ultrathin film optical coatings, *Nature Nanotechnology* **16**, 440 (2021).
- [11] S. Wieghold, J. Li, P. Simon, M. Krause, Y. Avlasevich, C. Li, J. A. Garrido, U. Heiz, P. Samorì, K. Müllen, F. Esch, J. V. Barth, and C.-A. Palma, Photoresponse of supramolecular self-assembled networks on graphene–diamond interfaces, *Nature Communications* **7**, 10700 (2016).
- [12] A. Al-Ashouri, E. Köhnen, B. Li, A. Magomedov, H. Hempel, P. Caprioglio, J. A. Márquez, A. B. M. Vilches, E. Kasparavicius, J. A. Smith, N. Phung, D. Menzel, M. Grischek, L. Kegelmann, D. Skroblin, C. Gollwitzer, T. Malinauskas, M. Jošt, G. Matič, B. Rech, R. Schlatmann, M. Topič, L. Korte, A. Abate, B. Stannowski, D. Neher, M. Stolterfoht, T. Unold, V. Getautis, and S. Albrecht, Monolithic perovskite/silicon tandem solar cell with > 29% efficiency by enhanced hole extraction, *Science* **370**, 1300 (2020).
- [13] X. Liu and M. C. Hersam, Interface Characterization and Control of 2D Materials and Heterostructures, *Advanced Materials* **30**, 1801586 (2018).
- [14] M. Gobbi, E. Orgiu, and P. Samorì, When 2D Materials Meet Molecules: Opportunities and Challenges of Hybrid Organic/Inorganic van der Waals Heterostructures, *Advanced Materials* **30**, 1706103 (2018).
- [15] R. Phillipson, C. J. L. d. I. Rosa, J. Teyssandier, P. Walke, D. Waghray, Y. Fujita, J. Adisojoso, K. S. Mali, I. Asselberghs, C. Huyghebaert, H. Uji-i, S. D. Gendt, and S. D. Feyter, Tunable doping of graphene by using physisorbed self-assembled networks, *Nanoscale* **8**, 20017 (2016).
- [16] A. J. Samuels and J. D. Carey, Molecular Doping and Band-Gap Opening of Bilayer Graphene, *ACS Nano* **7**, 2790 (2013).
- [17] B. Li, A. V. Klekachev, M. Cantoro, C. Huyghebaert, A. Stesmans, I. Asselberghs, S. D. Gendt, and S. D. Feyter, Toward tunable doping in graphene FETs by molecular self-assembled monolayers, *Nanoscale* **5**, 9640 (2013).
- [18] C. Coletti, C. Riedl, D. S. Lee, B. Krauss, L. Patthey, K. v. Klitzing, J. H. Smet, and U. Starke, Charge neutrality and band-gap tuning of epitaxial graphene on SiC by molecular doping, *Physical Review B* **81**, 235401 (2010), 0909.2966.
- [19] T. O. Wehling, K. S. Novoselov, S. V. Morozov, E. E. Vdovin, M. I. Katsnelson, A. K. Geim, and A. I. Lichtenstein, Molecular Doping of Graphene, *Nano Letters* **8**, 173 (2008), cond-mat/0703390.
- [20] W. Chen, S. Chen, D. C. Qi, X. Y. Gao, and A. T. S. Wee, Surface Transfer p-Type Doping of Epitaxial Graphene, *Journal of the American Chemical Society* **129**, 10418 (2007).
- [21] M. Fleischhauer, A. Imamoglu, and J. P. Marangos, Electromagnetically induced transparency: Optics in coherent media, *Reviews of Modern Physics* **77**, 633 (2005).
- [22] E. Malic, H. Appel, O. T. Hofmann, and A. Rubio, Förster-Induced Energy Transfer in Functionalized Graphene, *The Journal of Physical Chemistry C* **118**, 9283 (2014).
- [23] S. Park, N. Mutz, S. A. Kovalenko, T. Schultz, D. Shin, A. Aljarb, L. Li, V. Tung, P. Amsalem, E. J. W. List-Kratochvil, J. Stähler, X. Xu, S. Blumstengel, and N. Koch, Type-I Energy Level Alignment at the PTCDA—Monolayer MoS<sub>2</sub> Interface Promotes Resonance Energy Transfer and Luminescence Enhancement, *Advanced Science* **8**, 2100215 (2021).
- [24] J. V. Barth, G. Costantini, and K. Kern, Engineering atomic and molecular nanostructures at surfaces, *Nature* **437**, 671 (2005).
- [25] A. Ciesielski, C. Palma, M. Bonini, and P. Samorì, Towards Supramolecular Engineering of Functional Nanomaterials: Pre-Programming Multi-Component 2D Self-Assembly at Solid-Liquid Interfaces, *Advanced Materials* **22**, 3506 (2010).
- [26] A. Narita, X. Feng, Y. Hernandez, S. A. Jensen, M. Bonn, H. Yang, I. A. Verzhbitskiy, C. Casiraghi, M. R. Hansen, A. H. R. Koch, G. Fytas, O. Ivasenko, B. Li, K. S. Mali, T. Balandina, S. Mahesh, S. D. Feyter, and K. Müllen, Synthesis of structurally well-defined and liquid-phase-processable graphene nanoribbons, *Nature Chemistry* **6**, 126 (2014).
- [27] C. E. P. Villegas, P. B. Mendonça, and A. R. Rocha, Optical spectrum of bottom-up graphene nanoribbons: towards efficient atom-thick excitonic solar cells, *Scientific Reports* **4**, 6579 (2014), 1411.4204.
- [28] I. Ivanov, Y. Hu, S. Osella, U. Beser, H. I. Wang, D. Beljonne, A. Narita, K. Müllen, D. Turchinovich, and M. Bonn, Role of Edge Engineering in Photoconductivity of Graphene Nanoribbons, *Journal of the American Chemical Society* **139**, 7982 (2017).
- [29] S. Zhao, J. Lavie, L. Rondin, L. Orcin-Chaix, C. Diederichs, P. Roussignol, Y. Chassagneux, C. Voisin, K. Müllen, A. Narita, S. Campidelli, and J.-S. Lautret, Single photon emission from graphene quantum dots at room temperature, *Nature Communications* **9**, 3470 (2018), 1802.09870.
- [30] M. F. Limonov, M. V. Rybin, A. N. Poddubny, and Y. S. Kivshar, Fano resonances in photonics, *Nature Photonics* **11**, 543 (2017).
- [31] W. Zhou, D. Zhao, Y.-C. Shuai, H. Yang, S. Chuwongin, A. Chadha, J.-H. Seo, K. X. Wang, V. Liu, Z. Ma, and S. Fan, Progress in 2D photonic crystal Fano resonance photonics, *Progress in Quantum Electronics* **38**, 1 (2014).
- [32] M. F. Limonov, A. I. Rykov, S. Tajima, and A. Yamanaka, Superconductivity-induced effects on phononic and electronic Raman scattering in twin-free YBa<sub>2</sub>Cu<sub>3</sub>O<sub>7-x</sub> single crystals, *Physical Review B* **61**, 12412 (2000-5).
- [33] B. Luk'yanchuk, N. I. Zheludev, S. A. Maier, N. J. Halas, P. Nordlander, H. Giessen, and C. T. Chong, The Fano resonance in plasmonic nanostructures and metamaterials, *Nature Materials* **9**, 707 (2010).
- [34] M. Elstner, D. Porezag, G. Jungnickel, J. Elsner, M. Haugk, T. Frauenheim, S. Suhai, and G. Seifert, Self-consistent-charge density-functional tight-binding method for simulations of complex materials properties, *Physical Review B* **58**, 7260 (1998).
- [35] M. Gaus, Q. Cui, and M. Elstner, Density functional tight binding: application to organic and biological molecules, *Wiley Interdisciplinary Reviews: Computational Molecular Science* **4**, 49 (2014).
- [36] A. S. Christensen, T. Kubař, Q. Cui, and M. Elstner,

- Semiempirical Quantum Mechanical Methods for Noncovalent Interactions for Chemical and Biochemical Applications, *Chemical Reviews* **116**, 5301 (2016).
- [37] B. Hourahine, B. Aradi, V. Blum, F. Bonafé, A. Buccheri, C. Camacho, C. Cevallos, M. Y. Deshaye, T. Dumitrică, A. Dominguez, S. Ehlert, M. Elstner, T. v. d. Heide, J. Hermann, S. Irle, J. J. Kranz, C. Köhler, T. Kowalczyk, T. Kubař, I. S. Lee, V. Lutsker, R. J. Maurer, S. K. Min, I. Mitchell, C. Negre, T. A. Niehaus, A. M. N. Niklasson, A. J. Page, A. Pecchia, G. Penazzi, M. P. Persson, J. Řezáčs, C. G. Sánchez, M. Sternberg, M. Stöhr, F. Stuckenbergs, A. Tkatchenko, V. W.-z. Yu, and T. Frauenheim, DFTB+, a software package for efficient approximate density functional theory based atomistic simulations, *The Journal of Chemical Physics* **152**, 124101 (2020).
- [38] F. P. Bonafé, B. Aradi, B. Hourahine, C. R. Medrano, F. J. Hernández, T. Frauenheim, and C. G. Sánchez, A Real-Time Time-Dependent Density Functional Tight-Binding Implementation for Semiclassical Excited State Electron–Nuclear Dynamics and Pump–Probe Spectroscopy Simulations, *Journal of Chemical Theory and Computation* **16**, 4454 (2020).
- [39] C.-A. Palma, M. Awasthi, Y. Hernandez, X. Feng, K. Müllen, T. A. Niehaus, and J. V. Barth, Sub-Nanometer Width Armchair Graphene Nanoribbon Energy Gap Atlas, *The Journal of Physical Chemistry Letters* **6**, 3228 (2015).
- [40] C. Lian, M. Guan, S. Hu, J. Zhang, and S. Meng, Photoexcitation in Solids: First-Principles Quantum Simulations by Real-Time TDDFT, *Advanced Theory and Simulations* **1**, 1800055 (2018).
- [41] G. Stefanucci and R. v. Leeuwen, *Nonequilibrium Many-Body Theory of Quantum Systems* (Cambridge University Press, 2009).
- [42] J. Gersten and A. Nitzan, Electromagnetic theory of enhanced Raman scattering by molecules adsorbed on rough surfaces, *The Journal of Chemical Physics* **73**, 3023 (1980).
- [43] M. Barzan and F. Hajiesmaeilbaigi, Effect of gold nanoparticles on the optical properties of Rhodamine 6G, *The European Physical Journal D* **70**, 121 (2016).
- [44] Y. Cheng, T. Stakenborg, P. V. Dorpe, L. Lagae, M. Wang, H. Chen, and G. Borghs, Fluorescence Near Gold Nanoparticles for DNA Sensing, *Analytical Chemistry* **83**, 1307 (2011).
- [45] Y. D. Yin, L. Gao, and C. W. Qiu, Electromagnetic Theory of Tunable SERS Manipulated with Spherical Anisotropy in Coated Nanoparticles, *The Journal of Physical Chemistry C* **115**, 8893 (2011).
- [46] H. Fang, C. Battaglia, C. Carraro, S. Nemsak, B. Ozdol, J. S. Kang, H. A. Bechtel, S. B. Desai, F. Kronast, A. A. Unal, G. Conti, C. Conlon, G. K. Palsson, M. C. Martin, A. M. Minor, C. S. Fadley, E. Yablonovitch, R. Maboudian, and A. Javey, Strong interlayer coupling in van der Waals heterostructures built from single-layer chalcogenides, *Proceedings of the National Academy of Sciences* **111**, 6198 (2014), 1403.3754.
- [47] E. V. Calman, M. M. Fogler, L. V. Butov, S. Hu, A. Mishchenko, and A. K. Geim, Indirect excitons in van der Waals heterostructures at room temperature, *Nature Communications* **9**, 1895 (2018), 1709.07043.

# Fano Resonance and Incoherent interlayer excitons in molecular van der Waals heterostructures

Carlos R. Lien-Medrano<sup>1</sup>, Franco P. Bonafé<sup>2</sup>, Chi Yung Yam<sup>3</sup>,

Carlos-Andres Palma<sup>4,5,\*</sup>, Cristián G. Sánchez<sup>6,†</sup> and Thomas Frauenheim<sup>3,1</sup>

<sup>1</sup>*Bremen Center for Computational Materials Science, Universität Bremen, Bremen, Germany*

<sup>2</sup>*Max Planck Institute for the Structure and Dynamics of Matter, Hamburg, Germany*

<sup>3</sup>*Shenzhen JL Computational Science and Applied Research Institute (CSAR), Shenzhen, China*

<sup>4</sup>*Institute of Physics, Chinese Academy of Sciences; Beijing, P.R. China.*

<sup>5</sup>*Department of Physics & IRIS Adlershof, Humboldt-Universität zur Berlin, Berlin, Germany*

<sup>6</sup>*Instituto Interdisciplinario de Ciencias Básicas, Universidad Nacional de Cuyo, Mendoza, Argentina and*

<sup>7</sup>*Beijing Computational Science Research Center, Beijing 100193, China*

## I. COMPUTATIONAL METHODS

### A. Real time time-dependent density tight-binding

We have used the DFTB+ package [1], an implementation of the DFTB method, to obtain the GS Hamiltonian ( $H_{GS}$ ) and overlap matrix ( $S$ ). Using the  $H_{GS}$  and the  $S$  matrix, we computed the the initial GS reduced single-electron density matrix ( $\rho$ ). The mio-1-1 DFTB parameters set was employed to obtain the electronic structure of all the structures presented in this work. In order to describe the electronic dynamics of the systems under study we need to extend the DFTB method to the time-domain (TD-DFTB). On the basis of a real-time propagation of  $\rho$  under the influence of a time-varying external field, we can obtain excited-state properties of the systems. This propagation is achieved through the numerical integration of the Liouville-von Neumann equation of motion in the non-orthogonal basis:

$$\dot{\rho} = -i(S^{-1}H\rho - \rho HS^{-1}).$$

For more details on the theoretical method and its computational implementation, please refer to Bonafé et al. [2]. By applying a perturbation in the shape of a Dirac delta to the Hamiltonian, within the linear response regime, we can obtain the absorption spectra of the sytems as follows. The dipole moment is given by:

$$\mu(t) = \int_0^\infty \alpha(t-\tau)E(\tau)d\tau,$$

where  $\alpha(t-\tau)$  is the polarizability along the axis over which the external field  $\mathbf{E}(\tau)$  is applied. After the deconvolution of the applied electric field, the frequency dependent polarizability  $\alpha$  can be obtained:

$$\alpha(\omega) = \frac{\mu(\omega)}{E(\omega)}$$

The imaginary part of the polarizability is proportional to the Absorption spectrum.

For the study of the charge transfer processes, electron dynamics were triggered by the application of a continuous laser-type (sinusoidal) perturbation in tune with the excitation energy of interest.

---

\* Corresponding author.

palma@palmaland.edu

† Corresponding author.

csanchez@mendoza-conicet.gob.ar

## B. Derivation of the adapted Gersten-Nitzan model

Let  $A$  and  $B$  be two coupled point-dipoles, as depicted in Figure 3 (a) of the main manuscript. They are separated in the  $x$  direction by a distance  $R_{AB}$ . Both systems are coupled to an external time-dependent electric field  $\vec{E}_{\text{ext}}(t)$ , which can have any polarization direction within the  $(x, y)$  plane. Moreover, both systems are affected by the dipolar electric field generated by the other system. In other words, being  $\vec{E}_A$  and  $\vec{E}_B$  the effective electric fields acting on both systems,

$$\begin{aligned}\vec{E}_A(t) &= \vec{E}_{\text{ext}}(t) + \vec{E}_{BA}(\vec{R}_A, t) \\ \vec{E}_B(t) &= \vec{E}_{\text{ext}}(t) + \vec{E}_{AB}(\vec{R}_B, t)\end{aligned}$$

where  $\vec{E}_{BA}$  and  $\vec{E}_{AB}$  are the electric field generated by  $B$  acting on  $A$ , and the one generated by  $A$  acting on  $B$ , respectively, defined as:

$$\vec{E}_{BA}(R_A, t) = \int_{-\infty}^t \tilde{\chi}_B(\vec{R}_A, t, t') \vec{E}_{\text{ext}}(t') dt' \quad (1)$$

$$\vec{E}_{AB}(R_B, t) = \int_{-\infty}^t \tilde{\chi}_A(\vec{R}_B, t, t') \vec{E}_{\text{ext}}(t') dt' \quad (2)$$

Here,  $\tilde{\chi}$  is a **dipole-field response function** that is such that when multiplied by the external field and integrated yields the local dipole electric field generated by the system. It has a connection with the dipole susceptibility, which will be explored below. We start with the formula for the electric field of a perfect dipole, and being  $\vec{\mu}_I$  be the dipole moment of system  $I$ :

$$\vec{E}_{BA} = \frac{1}{4\pi\epsilon_0} \frac{3(\vec{\mu}_B \cdot \hat{R}_{BA}) \hat{R}_{BA} - \vec{\mu}_B}{R_{BA}^3} \quad (3)$$

As usual,  $\vec{R}_{BA} = \vec{R}_A - \vec{R}_B$ . By construction of the model,  $\vec{R}_{BA} = -R_{AB}\hat{x}$ , which means  $\hat{R}_{BA} = -\hat{x}$ ; and  $\vec{R}_{AB} = R_{AB}\hat{x}$ , ergo  $\hat{R}_{AB} = \hat{x}$ . By inserting the position vectors into eq. 3, we get:

$$\vec{E}_{BA} = \frac{1}{4\pi\epsilon_0} \frac{2\mu_{B_x}\hat{x} - \mu_{B_y}\hat{y}}{R_{AB}^3} \quad (4)$$

Now, by definition of the dipole response function  $\chi$ , and neglecting image field effects,

$$\vec{\mu}_B(t) = \vec{\mu}_B^0 + \int_{-\infty}^t \chi^B(t, t') \vec{E}_{\text{ext}}(t') dt' \quad (5)$$

Inserting 5 into 4:

$$\vec{E}_{BA} = \int_{-\infty}^t \frac{1}{4\pi\epsilon_0 R_{AB}^3} \begin{pmatrix} 2 & 0 \\ 0 & -1 \end{pmatrix} \cdot \chi^B(t, t') \cdot \vec{E}_{\text{ext}}(t') dt' \quad (6)$$

which by comparison with 1, allows us to define  $\tilde{\chi}$  for system  $B$ :

$$\tilde{\chi}_B = \frac{1}{4\pi\epsilon_0 R_{AB}^3} \begin{pmatrix} 2 & 0 \\ 0 & -1 \end{pmatrix} \chi^B(t, t') \quad (7)$$

As everything is symmetric under the exchange of labels  $A \rightarrow B$  and  $B \rightarrow A$ , we get now for  $\vec{E}_{AB}$  and  $\tilde{\chi}_A$  the following:

$$\vec{E}_{AB} = \int_{-\infty}^t \frac{1}{4\pi\epsilon_0 R_{AB}^3} C \chi^A(t, t') \cdot \vec{E}_{\text{ext}}(t') dt' \quad (8)$$

$$\tilde{\chi}_A = \frac{1}{4\pi\epsilon_0 R_{AB}^3} \begin{pmatrix} 2 & 0 \\ 0 & -1 \end{pmatrix} \chi^A(t, t') \quad (9)$$

Our goal is to get the polarizability of the combined system under the effect of the external field and of the dipolar field induced in the neighbour system, using as inputs the polarizabilities of the isolated systems. Then, we need to calculate both terms of the total dipole  $\vec{\mu}(t) = \vec{\mu}_A(t) + \vec{\mu}_B(t)$ . Starting with  $\vec{\mu}_A(t)$ , we have the the external field and the induced dipolar field terms:

$$\vec{\mu}_A(t) = \int_{-\infty}^t dt' \chi^A(t, t') \vec{E}_{\text{ext}}(t') + \int_{-\infty}^t \int_{-\infty}^{t'} dt' dt'' \chi^A(t, t') D \chi^B(t', t'') \vec{E}_{\text{ext}}(t'') \quad (10)$$

where  $D := \frac{1}{4\pi\epsilon_0 R_{AB}^3} \begin{pmatrix} 2 & 0 \\ 0 & -1 \end{pmatrix}$  is the geometrical factor. Calculating the Fourier transform of 10:

$$\vec{\mu}_A(\omega) = [\alpha^A(\omega) + \alpha^A(\omega) D \alpha^B(\omega)] \vec{E}(\omega) \quad (11)$$

And equivalently for  $B$ :

$$\vec{\mu}_B(\omega) = [\alpha^B(\omega) + \alpha^B(\omega) D \alpha^A(\omega)] \vec{E}(\omega) \quad (12)$$

These expressions suggest a natural definition of an effective polarizability, which can be written as:

$$\alpha^{\text{eff},A} = \alpha^A(\omega) + \alpha^A(\omega) D \alpha^B(\omega) \quad (13)$$

$$\alpha^{\text{eff},B} = \alpha^B(\omega) + \alpha^B(\omega) D \alpha^A(\omega) \quad (14)$$

Which is the formula used to calculate the polarizability components shown in Figure 3 of the main manuscript.

## II. FIGS. S1 TO S6

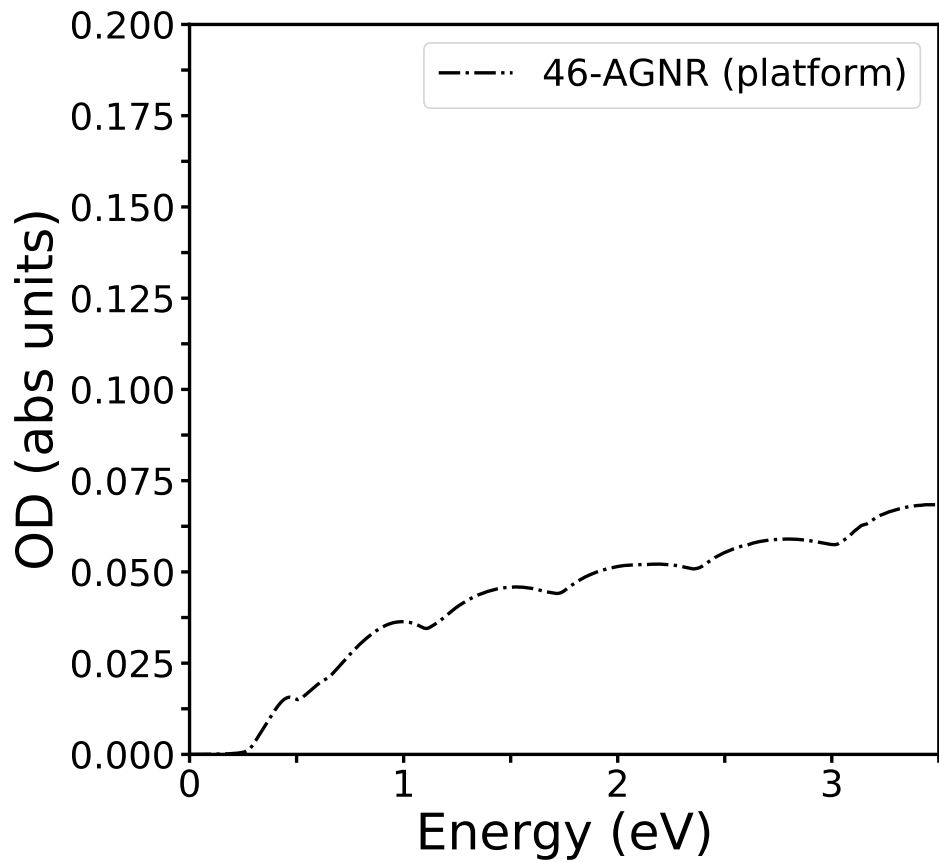


**Fig. S1. Absorption spectrum of 46-AGNR.**

The figure shows the absorption spectrum of the 46 atom width Armchair graphene nanoribbon (46-AGNR) used as the platform on the van der Waals molecular heterostructure presented in this work.

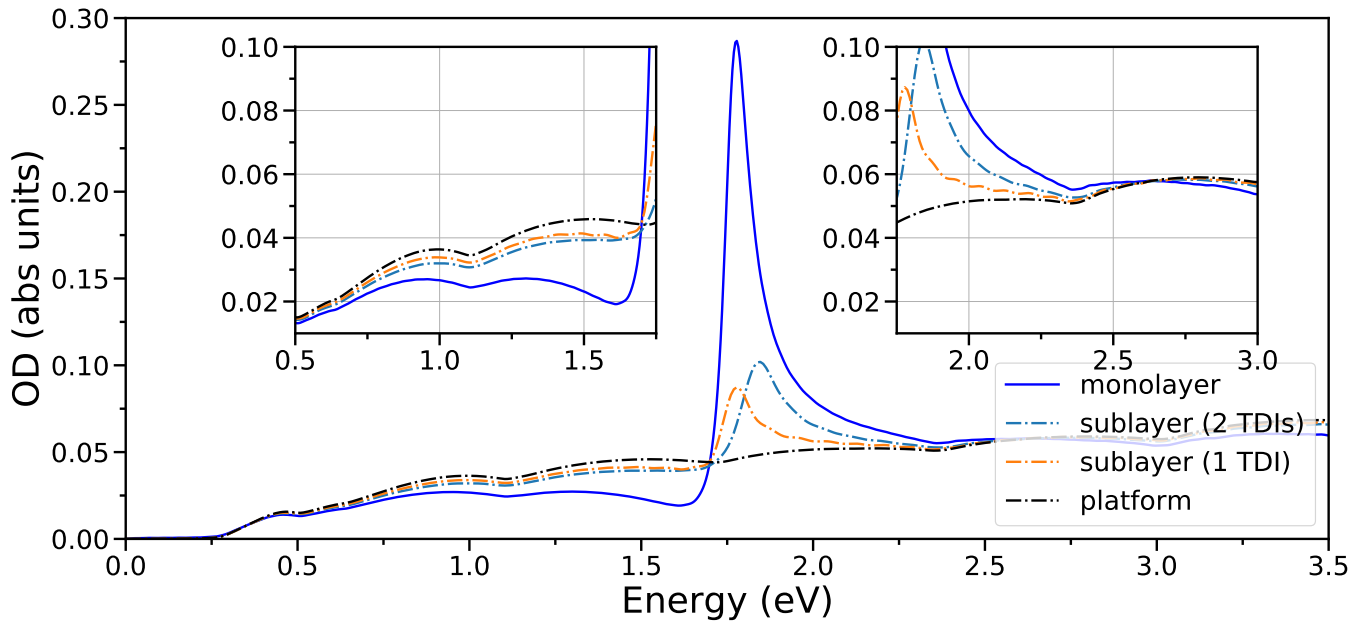


**Fig. S2 Coverage absorption dependency.** The absorption spectrum different sublayers of TDI molecules on top of the ribbon platform.

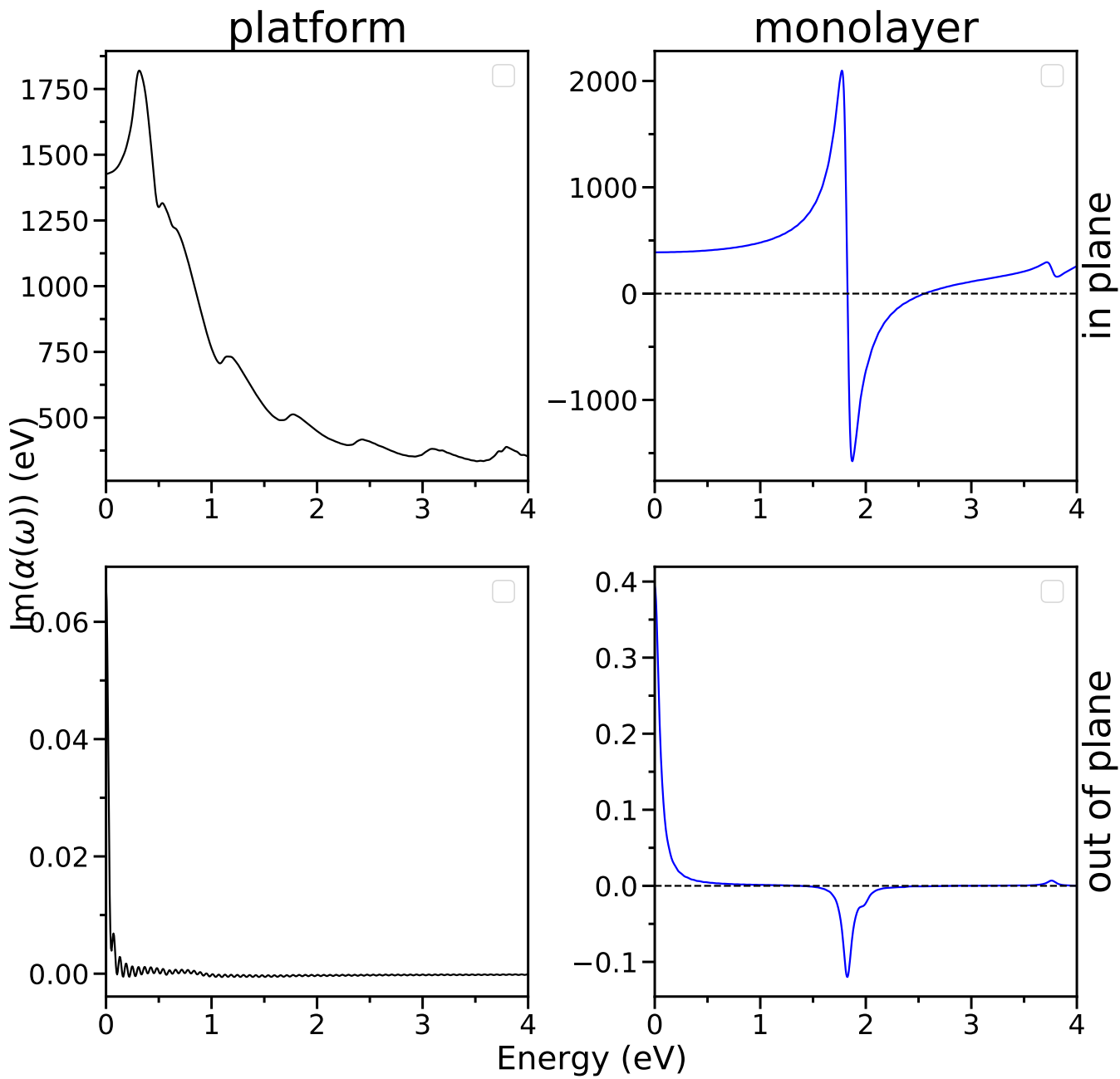


**Fig. S3. Individual polarizabilities for system 1a.** (A) In plane and out of plane polarizabilities for the platform. (B) In plane and out of plane polarizabilities for the monolayer of molecule 1.

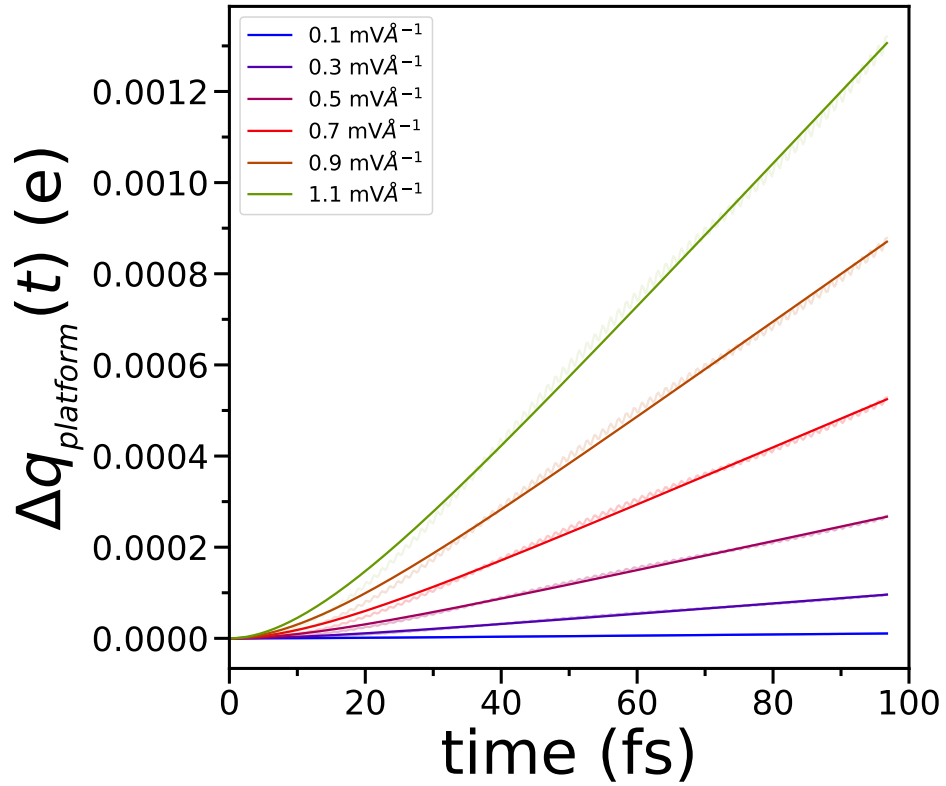


**Fig. S4.** Charge transfer  $\Delta q(t)$  of the platform for different field strengths as obtained from the dynamical simulations.

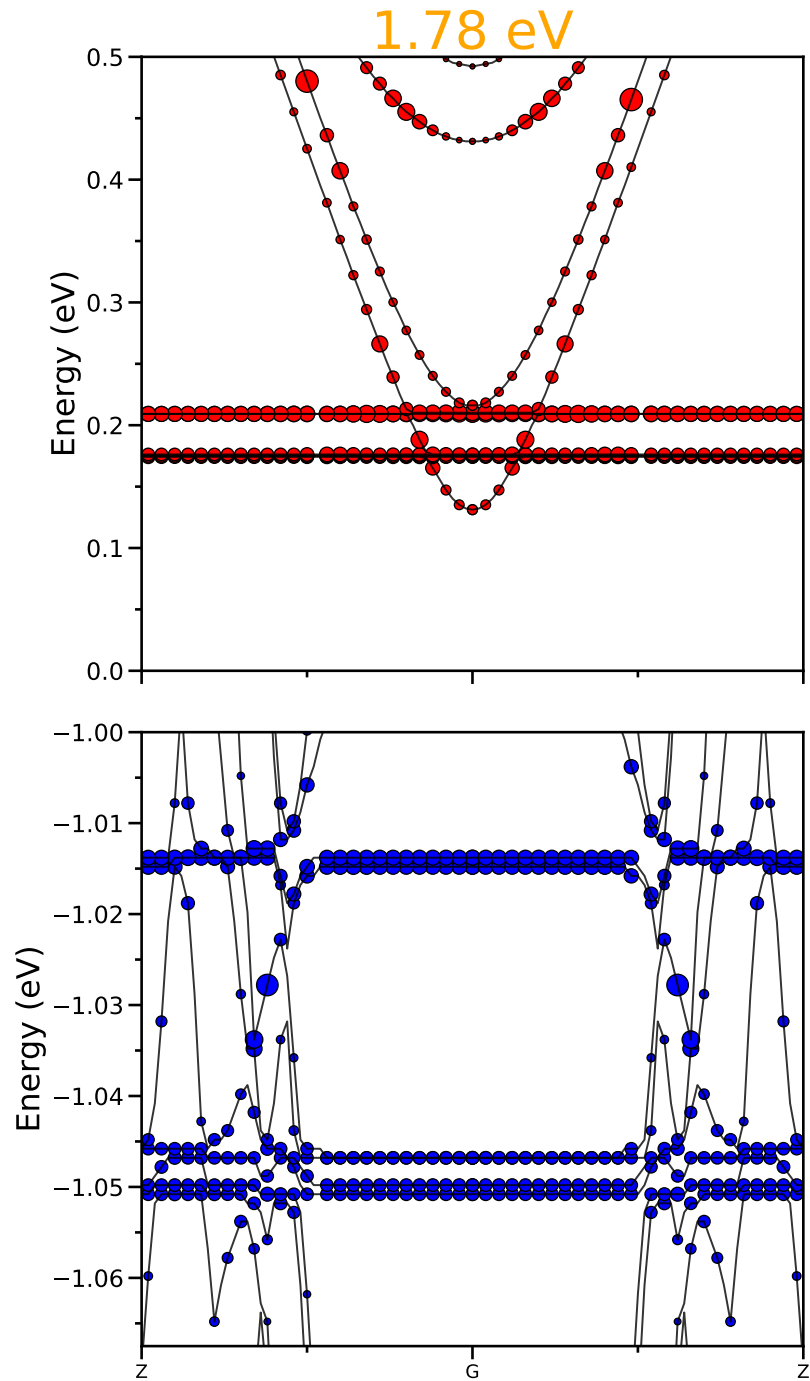


**Fig. S5. Detail of Fig. 2c** showing the band structure and populations for excitation at 1.78 in the energy regions corresponding to the HOMO and LUMO orbitals of the monolayer. Red (blue) circles denote the increase (decrease) of electron occupation and the circle size is proportional to the change of population.

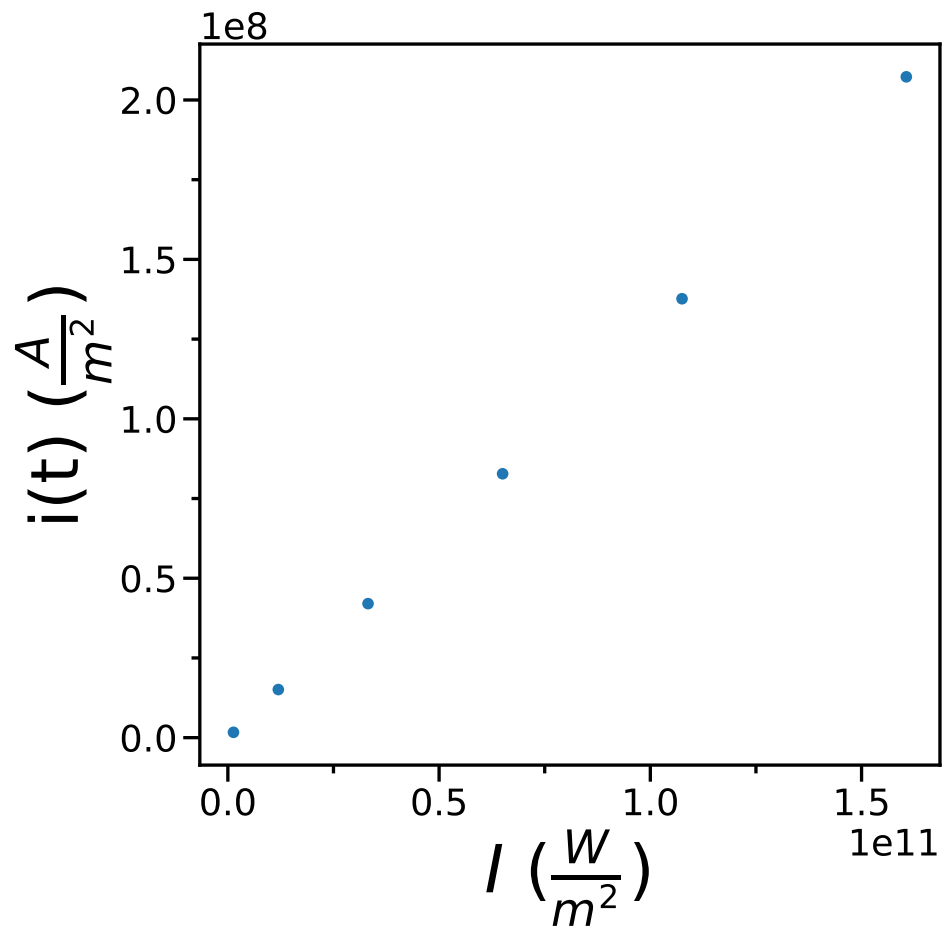


**Fig. S6. Photoresponse shown as interlayer current as a function of laser intensity.** Currents where obtained from the stationary state (linear) portion of the time dependent charge shown in Figure S4.

- 
- [1] B. Hourahine, B. Aradi, V. Blum, F. Bonafé, A. Buccheri, C. Camacho, C. Cevallos, M. Y. Deshaye, T. Dumitrică, A. Dominguez, S. Ehlert, M. Elstner, T. v. d. Heide, J. Hermann, S. Irle, J. J. Kranz, C. Köhler, T. Kowalczyk, T. Kubář, I. S. Lee, V. Lutsker, R. J. Maurer, S. K. Min, I. Mitchell, C. Negre, T. A. Niehaus, A. M. N. Niklasson, A. J. Page, A. Pecchia, G. Penazzi, M. P. Persson, J. Řezáćs, C. G. Sánchez, M. Sternberg, M. Stöhr, F. Stuckenbergs, A. Tkatchenko, V. W.-z. Yu, and T. Frauenheim, DFTB+, a software package for efficient approximate density functional theory based atomistic simulations, *The Journal of Chemical Physics* **152**, 124101 (2020).
  - [2] F. P. Bonafé, B. Aradi, B. Hourahine, C. R. Medrano, F. J. Hernández, T. Frauenheim, and C. G. Sánchez, A Real-Time Time-Dependent Density Functional Tight-Binding Implementation for Semiclassical Excited State Electron–Nuclear Dynamics and Pump–Probe Spectroscopy Simulations, *Journal of Chemical Theory and Computation* **16**, 4454 (2020).